Received: 9 March 2021 | Accepted: 14 April 2021

DOI: 10.1111/jace.17860

Journal of the American Ceramic Society

ORIGINAL ARTICLE

Electronic structure and thermal conductivity of zirconium carbide with hafnium additions

Yue Zhou | **William G. Fahrenholtz** | **Joseph Graham** | **Gregory E. Hilmas**

Department of Materials Science and Engineering, Missouri University of Science and Technology, Rolla, MO, USA

Correspondence
Yue Zhou, Department of Materials Science and Engineering, Missouri University of Science and Technology, Rolla, MO 65409, USA.
Email: yznwb@mst.edu

Funding information
U.S. National Science Foundation, Grant/Award Number: DMR 1742086

Abstract

The lattice thermal conductivity of ZrC with different Hf contents was investigated theoretically. The density of states and electron density differences were calculated for ZrC and (Zr,Hf)C containing 3.125 or 6.25 at% Hf. It was found that the electronic structure did not change significantly with the Hf additions. Lattice thermal conductivities were calculated for all of the compositions by combining first-principles calculations with the Debye–Callaway model. The theoretical lattice thermal conductivity of ZrC was 68 $W \cdot m^{-1} \cdot K^{-1}$ at room temperature. When adding 3.125 and 6.25 at% Hf into ZrC, the lattice thermal conductivities decreased to 18 and 15 $W \cdot m^{-1} \cdot K^{-1}$, respectively. The mechanism for the decreased conductivity is that with the addition of Hf impurities, the frequency of the acoustic phonons decreased, which resulted in decreases in the Debye temperature and lattice thermal conductivity.

KEYWORDS

first principles theory, thermal conductivity, zirconium/zirconium compounds

1 | INTRODUCTION

Zirconium carbide is a promising material for potential use in tristructural isotropic (TRISO) fuel particles[1] that will be used in advanced high temperature nuclear reactors.[2,3] The coolant outlet temperature of the very high temperature reactor (VHTR) concept is around 1000°C. To optimize the performance of TRISO fuel particles, zirconium carbide is being considered as an alternative to the silicon carbide layer. Zirconium carbide is structurally stable at the predicted operating temperatures and has favorable thermal conductivity, fission product retention characteristics, and radiation damage resistance. Zircon (nominally $ZrSiO_4$) is a naturally occurring mineral and is the principal raw material used in the commercial production of zirconium. Typically, zircon contains about 2 wt% of hafnium.[4] In practice, separating hafnium from zirconium is difficult because they have similar atomic radii, valence electron configurations, and chemical properties.[5] Therefore, Hf impurity is an important defect in ZrC and other zirconium compounds.

It is well-known that solid solution additions generally decrease the thermal conductivities of the resulting alloys. For example, the thermal conductivity of Ge–Si alloys is lower than that for either pure element.[6] The thermal conductivity of $Si_{0.7}Ge_{0.3}$ is about 6.3 $W \cdot m^{-1} \cdot K^{-1}$, which is lower than either pure Si (about 88 $W \cdot m^{-1} \cdot K^{-1}$) or pure Ge (about 50 $W \cdot m^{-1} \cdot K^{-1}$). The thermal conductivities of Mg alloys also decrease as the amount of alloying elements increases.[7–11] Likewise, the thermal conductivity of (Zr,Hf)NiSn half-Heusler alloys decreases when Ti is substituted onto the (Zr,Hf) sites or by substituting Sb onto Sn sites.[12] Solid solutions of yttria-stabilized hafnia-zirconia have lower thermal conductivities than either yttria-stabilized zirconia (YSZ) or yttria-stabilized hafnia end members. Replacement of Zr^{4+} ions on the zirconia sublattice with Hf^{4+} ions decreases the phonon mean free path.[13] For Al alloys, the thermal conductivities of binary Al alloys (Al–Si, Al–Cu, Al–Fe, and Al–Mg) are all lower than that of 99.8% pure Al.[14] The thermal conductivity of Al–Cu decreases as Cu content increases due to the scattering of electrons and phonons.[15] The thermal conductivity of Al–Si foundry alloys decreases due to

the addition of the main alloying elements of Si, Cu, and Ni.[16] Some theoretical studies found that solid solutions of $Mg_2Si_xSn_{1-x}$ had bulk thermal conductivities that were smaller than bulk Mg_2Si and bulk Mg_2Sn.[17] Similarly, lattice thermal conductivities of $Ti_xHf_{1-x}NiSn$ and $Zr_xHf_{1-x}NiSn$ half-Heusler alloys are lower than those for TiNiSn, ZrNiSn, and HfNiSn due to the mass disorder effect.[18]

Thermal conductivities of ceramic solid solutions have been studied experimentally. Thermal conductivities of high entropy carbides and high entropy borides are lower than the constituent transition metal carbides and borides.[19–22] The thermal conductivity of YSZ can be reduced by decreasing the grain size[23] and by doping with rare-earth oxides.[24] The thermal conductivity of Si also decreases with decreasing grain size (i.e., increasing density of grain boundaries) and due to increasing impurity content, both of which scatter phonons.[25,26] Irradiation has been shown to reduce the thermal conductivity of CeO_2,[27] SiC, Al_2O_3, $MgAl_2O_4$, AlN, Si_3N_4, and BeO[28] due to defects formation. Grain boundaries of $Y_3Al_5O_{12}$ also scatter phonons and reduce thermal conductivity.[29] Theory-based analysis provides an excellent complement to experimental results and can help provide insight into mechanisms controlling the observed behavior. Several recent studies have used the Debye–Callaway model with parameters determined from first-principles calculations to calculate lattice thermal conductivity for materials including selenium compounds,[30] γ-Si_3N_4, γ-Ge_3N_4,[31] and ZrB_2.[32] Previous experimental studies of the thermal conductivity of ZrC have resulted in values that range from about 26 to 42 $W{\cdot}m^{-1}{\cdot}K^{-1}$ at around 1500 K without a systematic explanation of the reasons for the differences.[33]

The purpose of this paper is to use theoretical methods to study the effect of hafnium content on the electronic structure and lattice thermal conductivity of (Zr,Hf)C solid solutions. Note that some of the results for pure ZrC used for comparison in the present study were from our previous study on the effect of carbon vacancy content on the thermal properties of ZrC_x ceramics.[34] The previously published results are shown in Figures 1A, 6A, and 7A as well as in Table 1.

2 | CALCULATION METHODS

2.1 | First-principles calculations

The valence electron configurations are $4d^25s^2$ for zirconium, $5d^26s^2$ for hafnium, and $2s^22p^2$ for carbon. The crystal structure of ZrC is rock salt (space group: $Fm\bar{3}m$, No. 225) with an initial lattice constant of 4.699 Å before geometry optimization as shown in Figure 1A. The atom coordinates are (0, 0, 0) for Zr and (0, 0.5, 0) for C with other atom positions generated based on symmetry operations. To investigate the effect of Hf on the electronic structure and thermal properties of ZrC, $2 \times 2 \times 2$ supercells of $(Zr_{1-x}Hf_x)C$ with $x = 3.125$ at%, hereafter written $Zr_{0.97}Hf_{0.03}C$, and $x = 6.250$ at%, hereafter written $Zr_{0.94}Hf_{0.06}C$, were built. The supercells were based on the ZrC unit cell with some Zr atoms replaced by Hf as shown in Figure 1B,C. The Hf atom positions were assigned to ensure that the structures of the supercells retained the cubic symmetry. The equilibrium crystal structures were optimized using the Broyden–Fletcher–Goldfarb–Shanno (BFGS) methodology.[35] The density of states, electron density differences, and phonon dispersion curves were

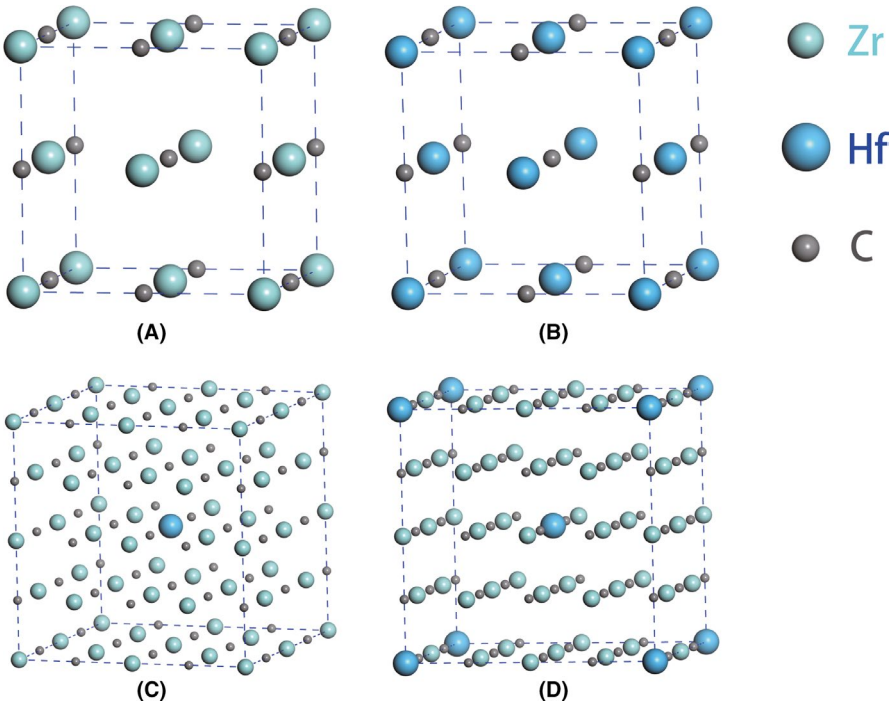

FIGURE 1 Crystal structures of (A) ZrC and (B) HfC and supercells of ZrC with (C) 3.125 at% Hf ($Zr_{0.97}Hf_{0.03}C$) and (D) 6.25 at% Hf ($Zr_{0.94}Hf_{0.06}C$) [Color figure can be viewed at wileyonlinelibrary.com]

TABLE 1 Group velocities, Debye temperature, and Grüneisen parameters of ZrC, HfC, $Zr_{0.97}Hf_{0.03}C$, and $Zr_{0.94}Hf_{0.06}C$

	v_{TA1}	v_{TA2}	v_{LA}	θ_{TA1}	θ_{TA2}	θ_{LA}	γ_{TA1}	γ_{TA2}	γ_{LA}
	Unit								
Composition	(km/s)			(K)			N/A		
ZrC	4.24	4.24	7.97	340	340	467	1.79	1.51	1.65
HfC	3.23	3.23	6.43	253	253	343	1.80	1.84	1.67
$Zr_{0.97}Hf_{0.03}C$	2.37	2.37	3.99	158	158	176	1.72	0.47	1.68
$Zr_{0.94}Hf_{0.06}C$	2.98	2.98	6.04	184	184	204	1.91	1.08	1.42

calculated from first principles using density function theory (DFT; Quantum Espresso).[36] Interactions between the ionic cores and the valence electrons were represented by Vanderbilt-type ultrasoft pseudopotentials.[37] The generalized-gradient approximation (GGA)[38] based on the Perdew–Burke–Ernzerhof (PBE) scheme was employed to treat the exchange-correlation energy. A plane-wave cutoff energy of 70 Ry was set after convergence tests. The special *k*-points sampling integration over the Brillouin zone was employed using the Monkhorst Pack method with $9 \times 9 \times 9$ spatial *k*-points mesh for ZrC and HfC and $4 \times 4 \times 4$ spatial *k*-points mesh for $Zr_{0.97}Hf_{0.03}C$ and $Zr_{0.94}Hf_{0.06}C$.[39] Phonon dispersion curves were calculated using density function perturbation theory.[40]

2.2 | Lattice thermal conductivity calculations

Lattice thermal conductivities (κ_l) were calculated at different temperatures using the Debye–Callaway model.[41] Two transverse (κ_{TA1} and κ_{TA2}) and one longitudinal (κ_{LA}) acoustic phonon modes contributed to the total lattice thermal conductivity (κ_l) as expressed by Equation (1):

$$\kappa_l = \kappa_{TA1} + \kappa_{TA2} + \kappa_{LA}. \tag{1}$$

In the present study, the contributions of optical phonons to lattice thermal conductivity were ignored due to the low group velocities of the optical phonons, which result in lower contributions to thermal conductivity than for acoustic modes.[42–44] Each of the acoustic branches (κ_i, where i represents TA1, TA2, and LA) gives rise to Debye–Callaway terms, which are expressed as

$$\kappa_{i1} = \frac{1}{3}\frac{k_B^4 T^3}{2\pi^2\hbar^3 v_i}\int_0^{\frac{\theta_i}{T}} \frac{\tau_C^i(x)\, x^4 e^x}{(e^x-1)^2}dx, \tag{2}$$

$$\kappa_{i2} = \frac{1}{3}\frac{k_B^4 T^3}{2\pi^2\hbar^3 v_i}\frac{\left[\int_0^{\frac{\theta_i}{T}} \frac{\tau_C^i(x)x^4e^x}{(e^x-1)^2}dx\right]^2}{\int_0^{\frac{\theta_i}{T}} \frac{\tau_C^i(x)x^4e^x}{\tau_N^i(x)\tau_R^i(x)(e^x-1)^2}dx}, \tag{3}$$

where k_B is the Boltzmann constant, $\hbar$ is the reduced Planck constant, and v_i is the group velocity of the acoustic phonons evaluated at the zone center. θ_i is the Debye temperature of the acoustic phonons, which is determined from $\theta_i = \hbar\omega_{max}/k_B$, where ω_{max} represents the maximum frequency of the acoustic phonon branches at the Brillouin zone boundary.[30] The factor x is determined by $x = \hbar\omega/k_B T$. In both Equations (2) and (3), τ_C is the total relaxation time for all phonon scattering processes. It is a combination of normal (N) and resistive (R) processes. The relaxation time for normal phonon processes is τ_N while τ_R is the sum of all the resistive scattering processes. Then, the total scattering rate is the sum of normal and resistive scattering rates, $\tau_C^{-1} = \tau_N^{-1} + \tau_R^{-1}$. The relaxation time for resistive processes is the sum of contributions from isotope scattering (τ_I^{-1}), grain boundary scattering (τ_B^{-1}), and Umklapp scattering (τ_U^{-1}).

Isotope scattering arises from random mass variations (from multi-isotope elements) at an atomic site in an otherwise perfect crystal. The scattering rate for isotope scattering can be expressed as[45]

$$\left[\tau_I^i\right]^{-1} = \frac{V k_B^4 \Gamma}{4\pi\hbar^4 v_L^3} x^4 T^4, \tag{4}$$

where Γ is the phonon-scattering parameter of the mass fluctuation as determined by

$$\Gamma = \sum_j c_j \left[\frac{m_j - \overline{m}}{\overline{m}}\right]^2, \tag{5}$$

with

$$\overline{m} = \sum_j c_j m_j, \tag{6}$$

where c_j and m_j are the natural abundances and masses of the constituent isotopes.

Grain boundary scattering is related to the phonon transit time between regularly spaced grain boundaries:

$$\left[\tau_B^i\right]^{-1} = \frac{v_i}{d}, \tag{7}$$

where d is the effective grain size. The grain boundary scattering rate is independent of temperature.

The Umklapp scattering rate can be expressed as[41]

$$\left[\tau_{\mathrm{U}}^{i}\right]^{-1} = \frac{\hbar\gamma_i^2}{Mv_i^2\theta_i}\left(\frac{k_{\mathrm{B}}}{\hbar}\right)^2 x^2T^3\exp\left(\frac{-\theta_i}{3T}\right), \quad (8)$$

where M is the average mass of atoms in the structure and γ_i is the Grüneisen parameter of the acoustic phonon branch, which is calculated by[46]

$$\gamma_i = \frac{\sum \gamma_{i,q}C_i(q)}{\sum C_i(q)}, \quad (9)$$

where $\gamma_{i,q}$ is the mode resolved Grüneisen parameter for mode i at wave vector q, which is determined by

$$\gamma_{i,q} = -\frac{\partial \ln\omega_{i,q}}{\partial \ln V}, \quad (10)$$

where V is the volume of the unit cell. In Equation (9), $C_i(q)$ is expressed as

$$C_i(q) = k_{\mathrm{B}}\left(\frac{\hbar\omega_{i,q}}{k_{\mathrm{B}}T}\right)^2 \frac{\exp\left(\frac{\hbar\omega_{i,q}}{k_{\mathrm{B}}T}\right)}{\left[\exp\left(\frac{\hbar\omega_{i,q}}{k_{\mathrm{B}}T}\right)-1\right]^2}. \quad (11)$$

The group velocities of the acoustic phonons are determined as

$$v_{\mathrm{g}}(i,q) = \frac{\partial\omega(i,q)}{\partial q}, \quad (12)$$

where the directional derivative of the dispersion is taken in the [100]. Low energy acoustic phonons have dispersion surfaces that are approximately conical. Therefore, group velocity is treated as isotropic.

3 | RESULTS AND DISCUSSION

3.1 | Electronic structure

The density of states for ZrC is shown in Figure 2A. A nonzero density of states at the Fermi level indicates the presence of metallic bonding in ZrC. From the partial density of states curves, the states at the Fermi level are mostly from the Zr 4*d* and C 2*p* states, demonstrating that the main contribution to electrical conductivity is from these states. The lowest lying states from −11.4 to −8.1 eV are mostly from quasi-core C 2*s* with small contributions from Zr 5*s*, Zr 4*p*, and Zr 4*d* orbitals, and they are not involved in chemical bonding. The states from −5.6 to −1.7 eV are mainly from overlapping of C 2*p* and Zr 4*d* orbitals, forming strong covalent bonds.

The density of states for $Zr_{0.97}Hf_{0.03}C$ and $Zr_{0.94}Hf_{0.06}C$ is shown in Figure 2B,C. The partial density of states for Hf is very similar to those of Zr in both compositions. Thus, the electronic structure and bonding properties of ZrC are not changed significantly when Hf is present in $Zr_{0.97}Hf_{0.03}C$ and $Zr_{0.94}Hf_{0.06}C$ solid solutions. However, in contrast to the presence of a small peak at the Fermi level in total density states of ZrC (Figure 2A), no peaks were present at Fermi level in the total density states of $Zr_{0.97}Hf_{0.03}C$ or $Zr_{0.94}Hf_{0.06}C$, indicating that both compositions are more stable than ZrC.

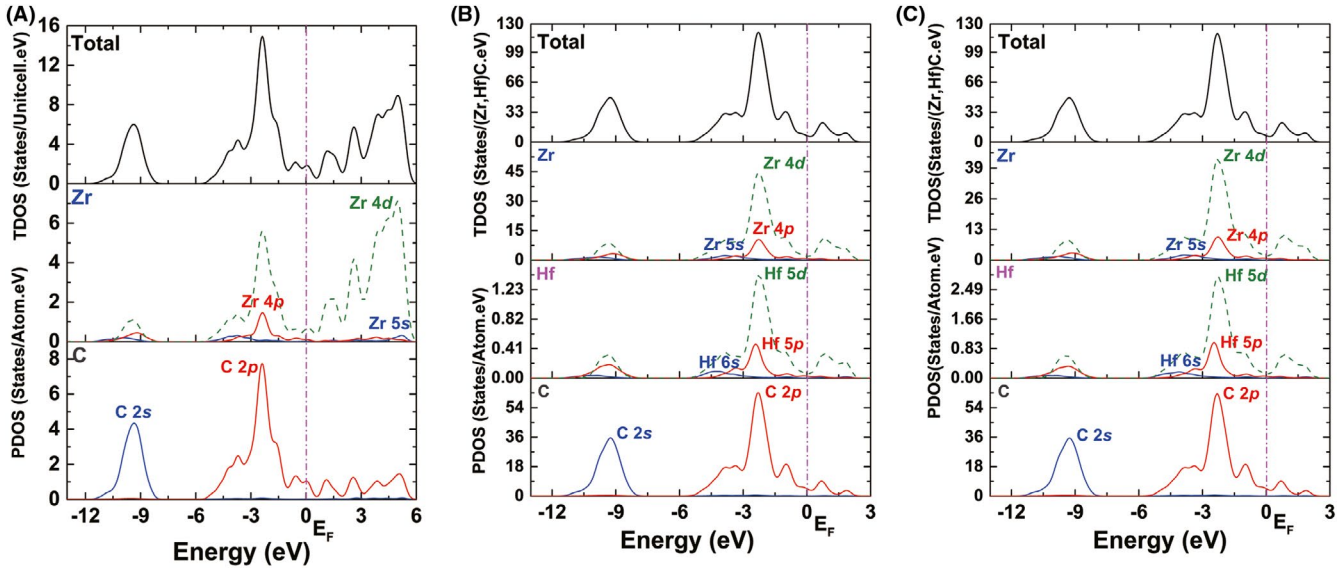

FIGURE 2 Density of states of (A) pure ZrC, (B) $Zr_{0.97}Hf_{0.03}C$, and (C) $Zr_{0.94}Hf_{0.06}C$ [Color figure can be viewed at wileyonlinelibrary.com]

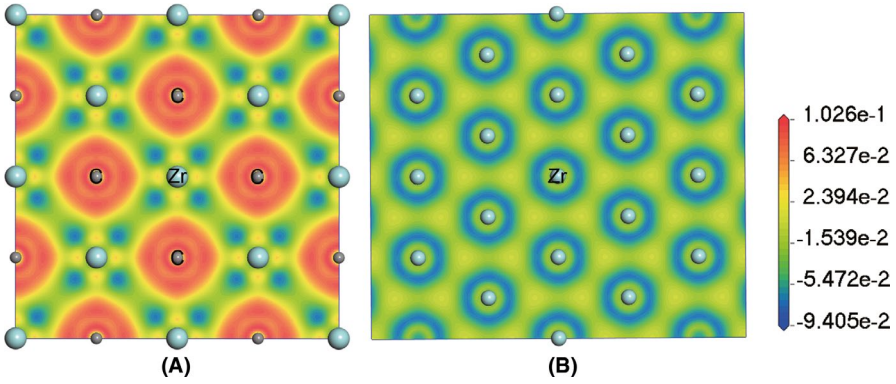

FIGURE 3 Electron density difference maps of ZrC on (A) (100) plane and (B) (111) plane. [Color figure can be viewed at wileyonlinelibrary.com]

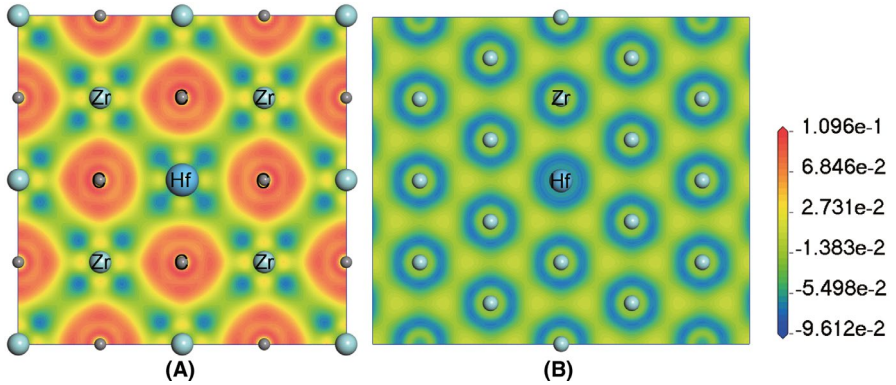

FIGURE 4 Electron density difference maps of $Zr_{0.97}Hf_{0.03}C$ on (A) (002) plane and (B) (111) plane [Color figure can be viewed at wileyonlinelibrary.com]

Electron density difference maps for ZrC are shown in Figure 3. The (100) and (111) planes were selected to study Zr–C and Zr–Zr bonds. On the (100) plane (Figure 3A), strong overlapping was obvious between the Zr $4de_g$ and C $2p_i$ (i represents the x, y, and z directions) orbitals, which indicates that strong covalent bonds form between Zr and C atoms. In addition, the electron density differences around the C atoms are not spherical, which indicates charge transfer from Zr to C. In other words, the Zr–C bonds have mixed covalent and ionic character. Typical metallic bonds between Zr atoms result in the triangular-shaped regions of higher electron density difference between Zr atoms on the (111) plane of ZrC (Figure 3B).

Figures 4 and 5 show the electron density difference maps for $Zr_{0.97}Hf_{0.03}C$ and $Zr_{0.94}Hf_{0.06}C$. The (002) planes were selected becuase these planes contain Zr, Hf, and C atoms in both supercells. No significant differences were observed except that the ionic character was stronger in Zr–C bonds than in Hf–C bonds. Similar to ZrC, the (111) planes were selected to view the electron density differences between Zr–Zr and Zr–Hf pairs. The metallic bonds in $Zr_{0.97}Hf_{0.03}C$ and $Zr_{0.94}Hf_{0.06}C$ are similar to those in ZrC. Electron density difference maps indicate that the addition of Hf does not significantly change the electron structure of $Zr_{0.97}Hf_{0.03}C$ or $Zr_{0.94}Hf_{0.06}C$ compared to ZrC.

3.2 | Phonon dispersion and group velocity

Phonon dispersion curves and group velocities for ZrC, HfC, $Zr_{0.97}Hf_{0.03}C$, and $Zr_{0.94}Hf_{0.06}C$ are shown in Figure 6. In Figure 6A,B, ZrC and HfC have six phonon branches because the primitive cells contain one Zr or Hf atom and one C atom. In Figure 6C,D, $Zr_{0.97}Hf_{0.03}C$ and $Zr_{0.94}Hf_{0.06}C$ supercells were used in phonon calculations such that much more phonon branches are included in these figures. The low frequency branches (below 10 THz for ZrC and 8 THz for HfC) are acoustic phonons (colored lines), and the high frequency branches (above 10 THz for ZrC and 8 THz for HfC) are optical phonons (black lines). The gaps between the acoustic and optical phonon branches for ZrC (5.6 THz at the Γ point) and HfC (10.3 THz at the Γ point) were attributed to anisotropic bonding and the mass difference between the Zr and C atoms in ZrC and between the Hf and C atoms in HfC.[47] As regard Hf-contained ZrC, athough a number of extra phonon branches in Figure 6C,D existed due to the more atoms in the supercells, compared with ZrC and HfC, the deterioration in acoustic phonons of supercells is significant. As will be illustrated later, such deterioration has great impact on the Debye temperature and group velocity of acoustic phonons, which eventually shaped the thermal conductivity of ZrC with Hf impurity.

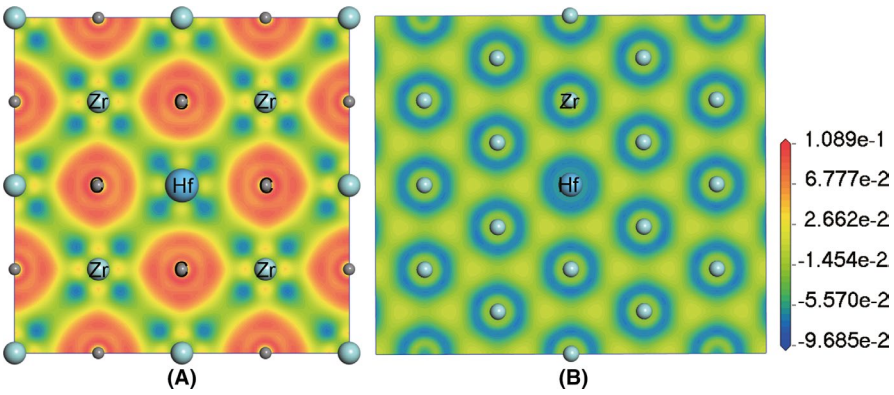

FIGURE 5 Electron density difference maps of $Zr_{0.94}Hf_{0.06}C$ on (A) (011) plane and (B) (111) plane [Color figure can be viewed at wileyonlinelibrary.com]

Group velocities were calculated for the acoustic phonons for all compositions. The group velocities are shown in Figure 6 beside the corresponding phonon dispersion curves, and the values are compiled in Table 1. Group velocities of HfC (v_{TA1} = 3.23 km/s, v_{TA2} = 3.23 km/s, and v_{LA} = 6.43 km/s) are lower than the corresponding group velocities of ZrC (v_{TA1} = 4.24 km/s, v_{TA2} = 4.24 km/s, and v_{LA} = 7.97 km/s). HfC has lower group velocities because of its high atomic weight resulted lower acoustic phonon frequencies, which reduce the slope of the acoustic phonons according to Equation (12). Notably, the initial addition of 3 at% of Hf into the ZrC lattice decreased the group velocities compared with pure ZrC (for $Zr_{0.97}Hf_{0.03}C$, v_{TA1} = 2.37 km/s, v_{TA2} = 2.37 km/s, and v_{LA} = 3.99 km/s). When the Hf content increased to 6 at%, group velocities increased (for $Zr_{0.94}Hf_{0.06}C$, v_{TA1} = 2.98 km/s, v_{TA2} = 2.98 km/s, and v_{LA} = 6.04 km/s). Higher group velocities of $Zr_{0.94}Hf_{0.06}C$ reflect the higher acoustic phonon frequencies compared with $Zr_{0.97}Hf_{0.03}C$ as shown in Figure 6. The contributions of the optical phonon branches to the group velocities were ignored due to their low values compared with the contributions of the acoustic branch, especially for $Zr_{0.97}Hf_{0.03}C$. Lattice thermal conductivity is proportional to the square of phonon group velocity, which can be expressed as $K_s(\omega) = C_s(\omega)V_g(\omega)^2\tau(\omega)$.[41] Reduction of group velocity will, therefore, decrease lattice thermal conductivity.

3.3 | Debye temperature

Debye temperatures were determined from the maximum acoustic phonon frequencies (two transverse and one longitudinal) at the Brillouin zone boundaries. The Debye temperature for HfC (θ_{TA1} = 253 K, θ_{TA2} = 253 K, θ_{LA} = 343 K) was lower than those for ZrC (θ_{TA1} = 340 K, θ_{TA2} = 340 K, θ_{LA} = 467 K) as shown in Table 1. The lower Debye temperature of HfC was due to the lower acoustic phonon frequencies. The addition of 3 at% Hf into ZrC reduced the Debye temperature (for $Zr_{0.97}Hf_{0.03}C$, θ_{TA1} = 158 K, θ_{TA2} = 158 K, θ_{LA} = 176 K) due to scattering of acoustic phonons by low lying optical phonons as shown in Figure 6C,D. Increasing the Hf content to 6 at% in ZrC led to a small increase in the Debye temperature (for $Zr_{0.94}Hf_{0.06}C$, θ_{TA1} = 184 K, θ_{TA2} = 184 K, θ_{LA} = 204 K) as presented in Table 1. Overall, Hf impurity has negative effect on the Debye temperature in general. The elastic constants of $Zr_{0.94}Hf_{0.06}C$ (c_{11} = 470.2 GPa, c_{12} = 101.2 GPa, c_{44} = 156.8 GPa) were higher than $Zr_{0.97}Hf_{0.03}C$ (c_{11} = 467.7 GPa, c_{12} = 101.1 GPa, c_{44} = 156.6 GPa), which means $Zr_{0.94}Hf_{0.06}C$ has stronger chemical bonds. The stronger chemical bonds increased the acoustic phonon frequency and increased the Debye temperature of $Zr_{0.94}Hf_{0.06}C$ compared with $Zr_{0.97}Hf_{0.03}C$.

3.4 | Lattice thermal conductivity

Temperature-dependent lattice thermal conductivities of ZrC, HfC, $Zr_{0.97}Hf_{0.03}C$, and $Zr_{0.94}Hf_{0.06}C$ are shown in Figure 7. The grain size was assumed to be 5 μm (Table 2) for all calculations. In those plots, κ_{UI} is the lattice thermal conductivity for isotopically pure ZrC and HfC; κ_{UA} is the lattice thermal conductivity with grain boundary effects; and κ_N represents the thermal conductivity with grain boundary effects plus Umklapp and normal phonon–phonon scattering processes. At room temperature, lattice thermal conductivities of ZrC were 122 $W{\cdot}m^{-1}{\cdot}K^{-1}$ for κ_{UI}, 100 $W{\cdot}m^{-1}{\cdot}K^{-1}$ for κ_{UA}, and 68 $W{\cdot}m^{-1}{\cdot}K^{-1}$ for κ_N. As discussed in our previous study,[33] these values are higher than experimentally measured values due to the assumption of no carbon vacancies, no impurities, and no porosity.

The lattice thermal conductivities of HfC (κ_{UI} = 83 $W{\cdot}m^{-1}{\cdot}K^{-1}$, κ_{UA} = 68 $W{\cdot}m^{-1}{\cdot}K^{-1}$, and κ_N = 47 $W{\cdot}m^{-1}{\cdot}K^{-1}$ at room temperature) were lower than ZrC, as expected from the lower group velocities. Typical experimental values for thermal conductivity of $HfC_{0.98}$ range from 20 to 25 $W{\cdot}m^{-1}{\cdot}K^{-1}$ at temperatures from 25 to 100°C.[48] Analogous to ZrC, the thermal conductivity of HfC predicted herein is higher than the experimental values, which are reduced by the defects in the sintered products[49–51] that are not accounted for in the modeling.

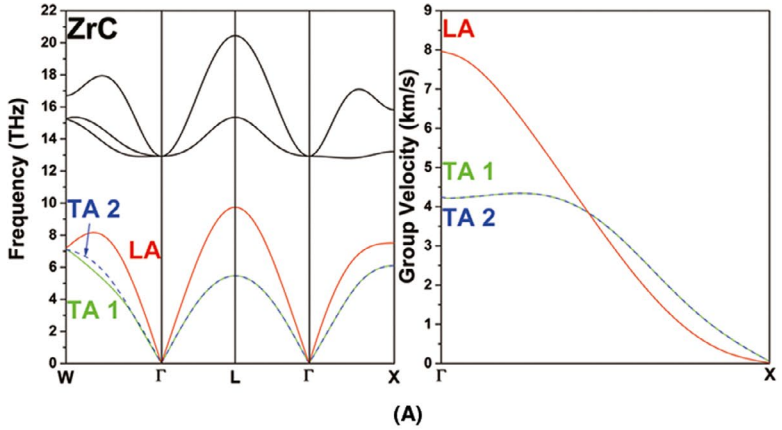

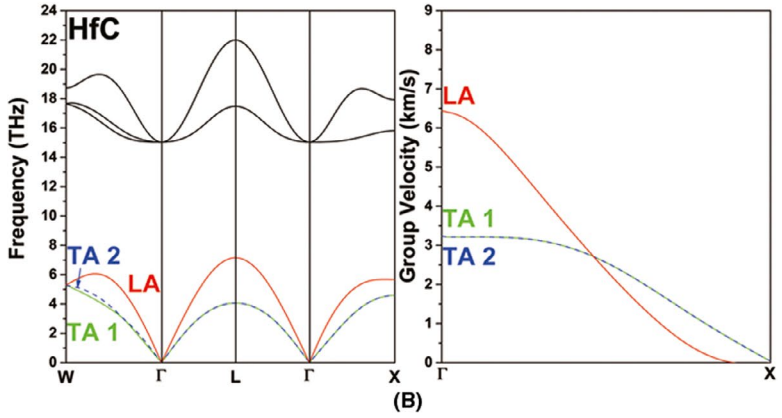

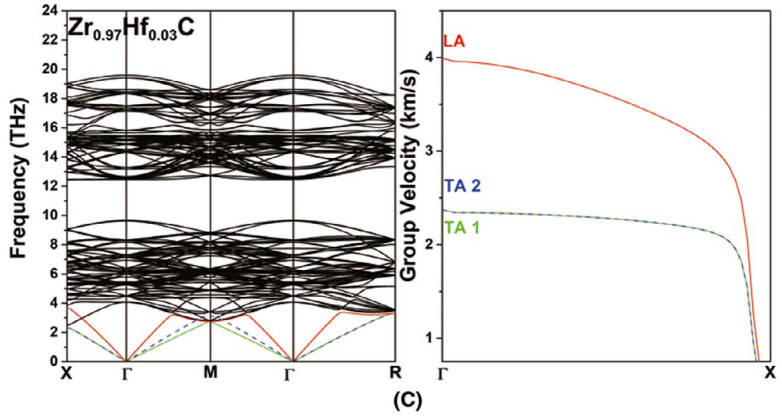

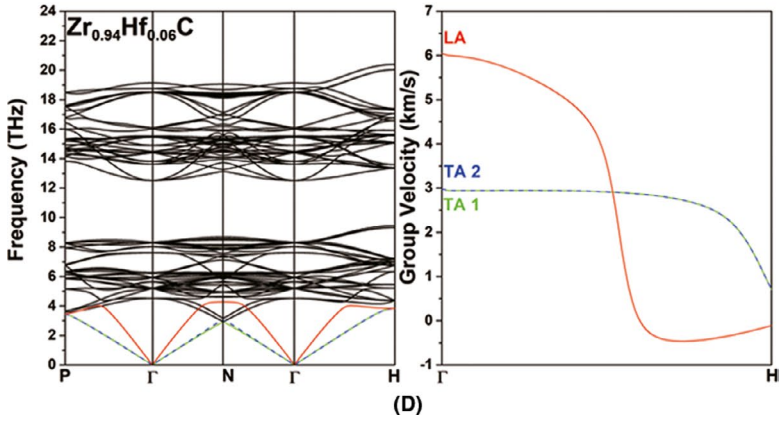

FIGURE 6 Phonon dispersions and group velocities of (A) ZrC and (B) HfC, (C) $Zr_{0.97}Hf_{0.03}C$, and (D) $Zr_{0.94}Hf_{0.06}C$ [Color figure can be viewed at wileyonlinelibrary.com]

TABLE 2 Average atomic masses, average grain diameters, and average atomic volumes of ZrC, HfC, $Zr_{0.97}Hf_{0.03}C$, and $Zr_{0.94}Hf_{0.06}C$

	Average atomic mass (a.u.)	Average diameter (μm)	Average atomic volume (Å^3)
ZrC	51.62	5	13.02
HfC	95.25	5	13.04
$Zr_{0.97}Hf_{0.03}C$	52.98	5	13.02
$Zr_{0.94}Hf_{0.06}C$	54.34	5	13.06

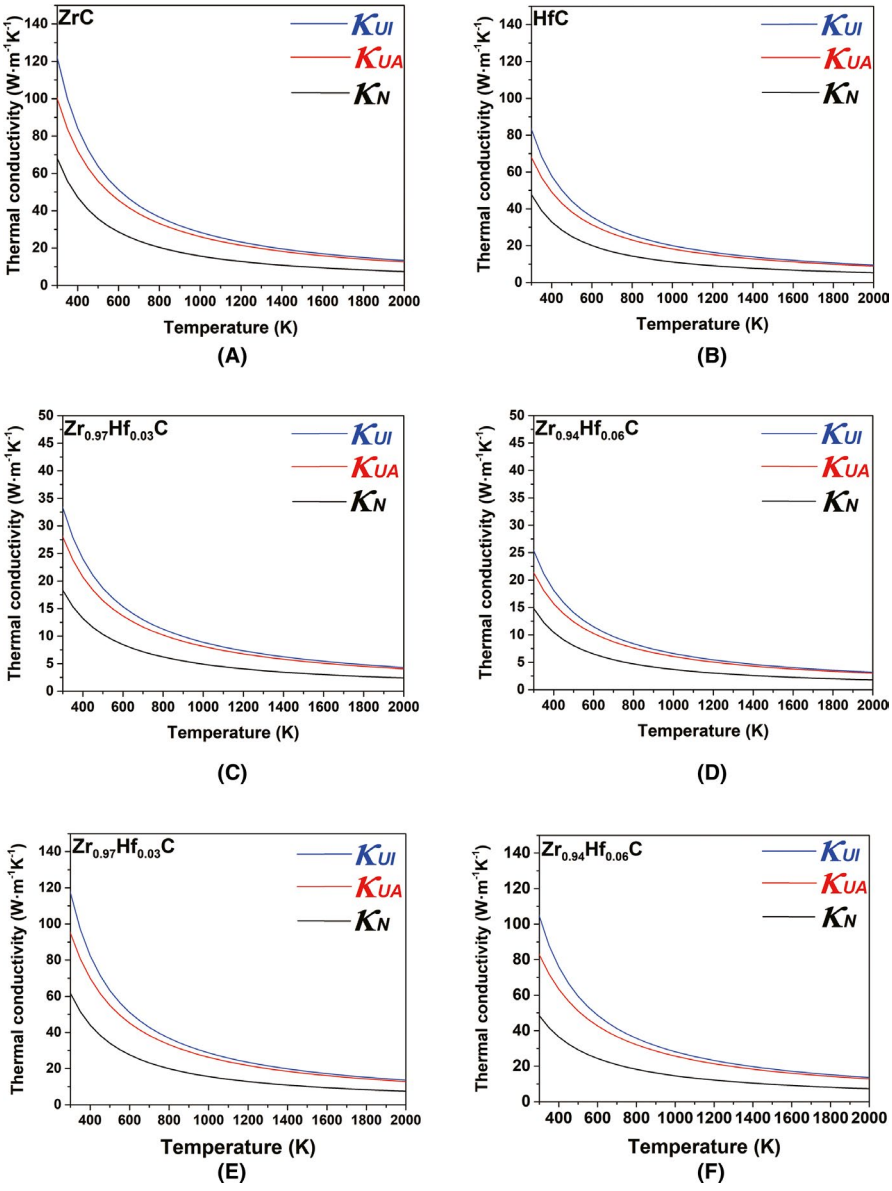

FIGURE 7 Lattice thermal conductivity of (A) ZrC, (B) HfC, (C) $Zr_{0.97}Hf_{0.03}C$, and (D) $Zr_{0.94}Hf_{0.06}C$. Hf was considered as isotope for (E) $Zr_{0.97}Hf_{0.03}C$ and (F) $Zr_{0.94}Hf_{0.06}C$. (κ_{UI} represents the lattice thermal conductivity, which considered as isotope effected; κ_{UA} represents the lattice thermal conductivity with isotope and grain boundary effects; κ_N represents the thermal conductivity with isotope and grain boundary effects, Umklapp, and normal phonon–phonon scattering) [Color figure can be viewed at wileyonlinelibrary.com]

After adding 3.125 at% of Hf into ZrC, the lattice thermal conductivity decreased compared with pure ZrC or pure HfC. At room temperature, κ_{UI} was 33 $W{\cdot}m^{-1}{\cdot}K^{-1}$, κ_{UA} was 28 $W{\cdot}m^{-1}{\cdot}K^{-1}$, and κ_N was 18 $W{\cdot}m^{-1}{\cdot}K^{-1}$ for $Zr_{0.97}Hf_{0.03}C$. The predicted lattice thermal conductivity values for $Zr_{0.94}Hf_{0.06}C$ at room temperature were $\kappa_{UI} = 25$ $W{\cdot}m^{-1}{\cdot}K^{-1}$, $\kappa_{UA} = 21$ $W{\cdot}m^{-1}{\cdot}K^{-1}$, and $\kappa_N = 15$ $W{\cdot}m^{-1}{\cdot}K^{-1}$, which were lower than $Zr_{0.97}Hf_{0.03}C$. Four effects contributed to the decrease in lattice thermal conductivity when Hf was added to ZrC. The first was the decrease in group velocity (Table 1). The spectral thermal conductivity is proportional to the square of the group velocity, $\kappa_s(\omega) = C_s(\omega)V_g(\omega)^2\tau(\omega)$[52]; therefore, decreasing group velocity leads to lower lattice thermal conductivity. The second reason was the decrease in Debye temperature (Table 1). According to Equations (2) and (3), decreasing Debye temperature decreases both acoustic

and optical phonon thermal conductivities; hence, the total lattice thermal conductivity is also decreased. Thirdly, the strain induced by the presence of Hf in the ZrC lattice decreased thermal conductivity. The Zr–C bond length (which was given after geometry optimization) for ZrC was 2.3524 Å, whereas the length of Hf–C bond was 2.3607 Å. After adding 3.125 at% Hf into ZrC, the average Zr–C bond length decreased to 2.3522 Å. Similarly, after adding 6.25 at% Hf to ZrC, the average Zr–C bond length was 2.3519 Å, whereas the average Hf–C bond was 2.3604 Å. The polarization of the bonds increases as the bond length increases due to the strain in the ZrC lattice after adding Hf, which leads to polarization scattering the phonons.[53] The final reason for the decrease in thermal conductivity is the increase in average atomic mass when Hf is added. The average atomic mass increased because Hf has a higher atomic mass than Zr. Increasing average atomic mass decreases the acoustic phonon frequencies and thereby decreases lattice thermal conductivity. Similar calculations were also performed by considering Hf as an isotope of Zr, and the lattice thermal conductivities were calculated as shown in Figure 7E,F. Lattice thermal conductivity decreased slightly compared with calculations that considered Hf to be and impurity with the same trend predicted by the other method.

4 | CONCLUSION

Electronic structures and lattice thermal conductivities were studied for ZrC and for ZrC containing Hf additions. The addition of Hf did not change the electronic structure of ZrC significantly. The lattice thermal conductivities were calculated with the Debye–Callaway model using Grüneisen parameters, Debye temperatures, and group velocities calculated from first principles. HfC has higher average Grüneisen parameters, lower Debye temperatures, and lower group velocities compared with ZrC. As expected, the lattice thermal conductivity of HfC (κ_N = 47 $W{\cdot}m^{-1}{\cdot}K^{-1}$ at room temperature) was lower than ZrC (κ_N = 68 $W{\cdot}m^{-1}{\cdot}K^{-1}$ at room temperature). With the addition of Hf into ZrC, the lattice thermal conductivities decreased to 18 $W{\cdot}m^{-1}{\cdot}K^{-1}$ for $Zr_{0.97}Hf_{0.03}C$ and 15 $W{\cdot}m^{-1}{\cdot}K^{-1}$ for $Zr_{0.94}Hf_{0.06}C$, respectively. The decrease in lattice thermal conductivity with the addition of Hf into the ZrC lattice was attributed to the decrease in frequencies of acoustic phonons, which, in turn, induced lower group velocities and Debye temperatures.

ACKNOWLEDGMENTS

This research was supported by the Ceramics Program in the Division of Materials Research at the U.S. National Science Foundation (DMR 1742086). The first principle calculation work was conducted with help by National Supercomputing Center in Shenzhen, China.

ORCID

Yue Zhou https://orcid.org/0000-0001-6901-947X
William G. Fahrenholtz https://orcid.org/0000-0002-8497-0092

REFERENCES

1. Ueta S, Aihara J, Yasuda A, Hideharu I, Takayama T, Sawa K. Fabrication of uniform ZrC coating layer for the coated fuel particle of the very high temperature reactor. J Nucl Mater. 2008;376(2):146–51.
2. Sabharwall P, Bragg-Sitton SM, Stoots C. Challenges in the development of high temperature reactors. Energy Convers Manag. 2013;74:574–81.
3. Fütterer MA, Fu LI, Sink C, de Groot S, Pouchon M, Kim YW, et al. Status of the very high temperature reactor system. Prog Nucl Energy. 2014;77:266–81.
4. Gambogi J. Zirconium and hafnium. Ind Miner. 1994:311.
5. Xu L, Xiao Y, Van Sandwijk A, Xu Q, Yang Y. Production of nuclear grade zirconium: a review. J Nucl Mater. 2015;466:21–8.
6. Abeles B, Beers DS, Cody GD, Dismukes JP. Thermal conductivity of Ge-Si alloys at high temperatures. Phys Rev. 1962;125(1):44.
7. Rudajevová A, Von Buch F, Mordike BL. Thermal diffusivity and thermal conductivity of MgSc alloys. J Alloys Compd. 1999;292(1–2):27–30.
8. Rudajevova A, Staněk M, Lukáč P. Determination of thermal diffusivity and thermal conductivity of Mg–Al alloys. Mater Sci Eng A. 2003;341(1–2):152–7.
9. Pan H, Pan F, Yang R, Peng J, Zhao C, She J, et al. Thermal and electrical conductivity of binary magnesium alloys. J Mater Sci. 2014;49(8):3107–24.
10. Su C, Li D, Ying T, Zhou L, Li L, Zeng X. Effect of Nd content and heat treatment on the thermal conductivity of MgNd alloys. J Alloys Compd. 2016;685:114–21.
11. Su C, Li D, Luo AA, Ying T, Zeng X. Effect of solute atoms and second phases on the thermal conductivity of Mg-RE alloys: a quantitative study. J Alloys Compd. 2018;747:431–7.
12. Sakurada S, Shutoh N. Effect of Ti substitution on the thermoelectric properties of (Zr, Hf) NiSn half-Heusler compounds. Appl Phys Lett. 2005;86(8):082105.
13. Winter MR, Clarke DR. Thermal conductivity of yttria-stabilized zirconia–hafnia solid solutions. Acta Mater. 2006;54(19):5051–9.
14. Chen JK, Hung HY, Wang CF, Tang NK. Thermal and electrical conductivity in Al–Si/Cu/Fe/Mg binary and ternary Al alloys. J Mater Sci. 2015;50(16):5630–9.
15. Wu J, Zhang H, Zhang Y, Li J, Wang X. Effect of copper content on the thermal conductivity and thermal expansion of Al–Cu/diamond composites. Mater Des. 2012;39:87–92.
16. Stadler F, Antrekowitsch H, Fragner W, Kaufmann H, Pinatel EF, Uggowitzer PJ. The effect of main alloying elements on the physical properties of Al–Si foundry alloys. Mater Sci Eng A. 2013;560:481–91.
17. Li W, Lindsay L, Broido DA, Stewart DA, Mingo N. Thermal conductivity of bulk and nanowire $Mg_2Si_xSn_{1-x}$ alloys from first principles. Phys Rev B. 2012;86(17):174307.
18. Eliassen SNH, Katre A, Madsen GKH, Persson C, Løvvik OM, Berland K. Lattice thermal conductivity of $Ti_xZr_yHf_{1-x-y}$ NiSn half-Heusler alloys calculated from first principles: Key role of nature of phonon modes. Phys Rev B. 2017;95(4):045202.

19. Yan X, Constantin L, Lu Y, Silvain JF, Nastasi M, Cui B. ($Hf_{0.2}Zr_{0.2}Ta_{0.2}Nb_{0.2}T_{i0.2}$) C high-entropy ceramics with low thermal conductivity. J Am Ceram Soc. 2018; 101(10): 4486–91.
20. Joshua G, Wright A, Quiambao-Tomko K, Qin M, Tomko JA, bin Hoque MS,, et al. Thermal conductivity and hardness of three single-phase high-entropy metal diborides fabricated by borocarbothermal reduction and spark plasma sintering. Ceram Int. 2020;46(5):6906–13.
21. Dai FZ, Wen B, Sun YJ, Xiang HM, Zhou YC. Theoretical prediction on thermal and mechanical properties of high entropy ($Zr_{0.2}Hf_{0.2}Ti_{0.2}Nb_{0.2}Ta_{0.2}$)C by deep learning potential. J Mater Sci Tech. 2020;43:168–74.
22. Dai FZ, Sun YJ, Wen B, Xiang HM, Zhou YC. Temperature dependent thermal and elastic properties of high entropy ($Ti_{0.2}Zr_{0.2}Hf_{0.2}Nb_{0.2}Ta_{0.2}$)$B_2$: molecular dynamics simulation by deep learning potential. J Mater Sci Tech. 2021;72:8–15.
23. Yang HS, Bai GR, Thompson LJ, Eastman JA. Interfacial thermal resistance in nanocrystalline yttria-stabilized zirconia. Acta Mater. 2002;50(9):2309–17.
24. Zhu D, Miller RA. Thermal conductivity and sintering behavior of advanced thermal barrier coatings. Nonmetallic Materials. NASA/TM-2002-211481, NAS 1.15:211481, E-13249. 2002. http://gltrs.grc.nasa.gov/GLTRS
25. Wang Z, Alaniz JE, Jang W, Garay JE, Dames C. Thermal conductivity of nanocrystalline silicon: importance of grain size and frequency-dependent mean free paths. Nano Lett. 2011;11(6):2206–13.
26. Bux SK. Synthesis and characterization of bulk nanostructured semiconductors for thermoelectric applications. Adv Funct Mater. 2009;19(25):2445–52.
27. Khafizov M, Pakarinen J, He L, Hurley DH. Impact of irradiation induced dislocation loops on thermal conductivity in ceramics. J Am Ceram Soc. 2019;102(12):7533–42.
28. Snead LL, Zinkle SJ, White DP. Thermal conductivity degradation of ceramic materials due to low temperature, low dose neutron irradiation. J Nucl Mater. 2005;340(2–3):187–202.
29. Bisson JF, Yagi H, Yanagitani T, Kaminskii A, Barabanenkov YN, Ueda KI, et al. Influence of the grain boundaries on the heat transfer in laser ceramics. Opt Rev. 2007;14(1):1–13.
30. Zhang Y. First-principles Debye-Callaway approach to lattice thermal conductivity. J Materiomics. 2016;2(3):237–47.
31. Xiang H, Feng Z, Li Z, Zhou Y. Theoretical investigations on mechanical and dynamical properties of MAlB (M = Mo, W) nanolaminated borides at ground-states and elevated temperatures. Sci Rep. 2018;8(1):1–9.
32. Xiang H, Wang J, Zhou Y. Theoretical predictions on intrinsic lattice thermal conductivity of ZrB_2. J Eur Ceram Soc. 2019;39(10):2982–8.
33. Katoh Y, Vasudevamurthy G, Nozawa T, Snead LL. Properties of zirconium carbide for nuclear fuel applications. J Nucl Mater. 2013;441(1–3):718–42.
34. Zhou Y, Fahrenholtz WG, Graham J, Hilmas GE. From thermal conductive to thermal insulating: effect of carbon vacancy content on lattice thermal conductivity of ZrC_x. J Mater Sci Technol. 2021;82:105–13.
35. Pfrommer BG, Côté M, Louie SG, Cohen ML. Relaxation of crystals with the quasi-Newton method. J Comput Phys. 1997;131(1):233–40.
36. Giannozzi P, Baroni S, Bonini N, Calandra M, Car R, Cavazzoni C, et al. QUANTUM ESPRESSO: a modular and open-source software project for quantum simulations of materials. J Phys Condens Matter. 2009;21(39):395502.
37. David V. Soft self-consistent pseudopotentials in a generalized eigenvalue formalism. Phys Rev B. 1990;41(11):7892–5.
38. Perdew JP, Burke K, Ernzerhof M. Generalized gradient approximation made simple. Phys Rev Lett. 1996;77(18):3865–8.
39. Monkhorst HJ, Pack JD. Special points for Brillouin-zone integrations. Phys Rev B. 1976;13(12):5188.
40. Gonze X. First-principles responses of solids to atomic displacements and homogeneous electric fields: implementation of a conjugate-gradient algorithm. Phys Rev B. 1997;55(16):10337.
41. Morelli DT, Heremans JP, Slack GA. Estimation of the isotope effect on the lattice thermal conductivity of group IV and group III-V semiconductors. Phys Rev B. 2002;66(19):195304.
42. Xiang H, Zhou Y. Phonon engineering in tuning the thermal conductivity of alkaline-earth hexaborides. J Eur Ceram Soc. 2020;40(4):1352–60.
43. Asen-Palmer M, Bartkowski K, Gmelin E, Cardona M, Zhernov AP, Inyushkin AV, et al. Thermal conductivity of germanium crystals with different isotopic compositions. Phys Rev B. 1997;56(15):9431–47.
44. Lindsay L, Broido DA, Reinecke TL. Phonon-isotope scattering and thermal conductivity in materials with a large isotope effect: a first-principles study. Phys Rev B. 2013;88(14):144306.
45. Klemens PG. The scattering of low-frequency lattice waves by static imperfections. Proc Phys Soc A. 1955;68(12):1113–28.
46. Grimvall G. Thermophysical Properties of Materials. Amsterdam, Netherlands: Elsevier; 1999.
47. Xiang H, Feng Z, Li Z, Zhou Y. First-principles investigations on elevated temperature elastic and thermodynamic properties of ZrB_2 and HfB_2. J Am Ceram Soc. 2017;100(8):3662–72.
48. Opeka MM, Talmy IG, Wuchina EJ, Zaykoski JA, Causey SJ. Mechanical, thermal and oxidation properties of refractory hafnium and zirconium compounds. J Eur Ceram Soc. 1999;19(13–14):2405–14.
49. Wuchina E, Opeka M, Causey S, Buesking K, Spain J, Cull A, et al. Designing for ultrahigh-temperature applications: the mechanical and thermal properties of HfB_2, HfC_x, HfN_x and αHf(N). J Mater Sci. 2004;39(19):5939–49.
50. Chen H, Xiang H, Dai F, Liu J, Zhou Y. Low thermal conductivity and high porosity ZrC and HfC ceramics prepared by in-situ reduction reaction/partial sintering method for ultrahigh temperature applications. J Mater Sci Technol. 2019;35(12):2778–84.
51. Shimada S, Inagaki M, Matsui K. Oxidation kinetics of hafnium carbide in the temperature range of 480 to 600°C. J Am Ceram Soc. 1992;75(10):2671–8.
52. Morelli D, Heremans J. Thermal conductivity of germanium-, silicon-, and carbon nitride. Appl Phys Lett. 2003;81(27):8–10.
53. Toberer ES, Zevalkink A, Snyder GJ. Phonon engineering through crystal chemistry. J Mater Chem. 2011;21(40):15843–52.

How to cite this article: Zhou Y, Fahrenholtz WG, Graham J, Hilmas GE. Electronic structure and thermal conductivity of zirconium carbide with hafnium additions. *J Am Ceram Soc*. 2021;104:4708–4717. https://doi.org/10.1111/jace.17860